Dispersion mismatch correction for evident chromatic anomaly in low coherence interferometry

View Online   Export Citation   CrossMark

Rishyashring R. Iyer,[1,2] (iD) Lingxiao Yang,[1,2] (iD) Janet E. Sorrells,[1,3] (iD) Eric J. Chaney,[1,4] (iD)
Darold R. Spillman, Jr.,[1,5] (iD) and Stephen A. Boppart[1,2,3,4,5,6,7,a)] (iD)

AFFILIATIONS

[1] Beckman Institute for Advanced Science and Technology, University of Illinois Urbana-Champaign, Urbana, Illinois 61801, USA
[2] Department of Electrical and Computer Engineering, University of Illinois Urbana-Champaign, Urbana, Illinois 61801, USA
[3] Department of Bioengineering, University of Illinois Urbana-Champaign, Urbana, Illinois 61801, USA
[4] Cancer Center at Illinois, University of Illinois Urbana-Champaign, Urbana, Illinois 61801, USA
[5] NIH/NIBIB P41 Center for Label-free Imaging and Multiscale Biophotonics (CLIMB), University of Illinois Urbana-Champaign, Urbana, Illinois 61801, USA
[6] Carle Illinois College of Medicine, University of Illinois Urbana-Champaign, Urbana, Illinois 61801, USA
[7] Interdisciplinary Health Sciences Institute, University of Illinois Urbana-Champaign, Urbana, Illinois 61801, USA

[a)] Author to whom correspondence should be addressed: boppart@illinois.edu. **Tel.**: (217) 244-7479.

ABSTRACT

The applications of ultrafast optics to biomedical microscopy have expanded rapidly in recent years, including interferometric techniques like optical coherence tomography and microscopy (OCT/OCM). The advances of ultra-high resolution OCT and the inclusion of OCT/OCM in multimodal systems combined with multiphoton microscopy have marked a transition from using pseudo-continuous broadband sources, such as superluminescent diodes, to ultrafast supercontinuum optical sources. We report anomalies in the dispersion profiles of low-coherence ultrafast pulses through long and non-identical arms of a Michelson interferometer that are well beyond group delay or third-order dispersions. This chromatic anomaly worsens the observed axial resolution and causes fringe artifacts in the reconstructed tomograms in OCT/OCM using traditional algorithms. We present DISpersion COmpensation Techniques for Evident Chromatic Anomalies (DISCOTECA) as a universal solution to address the problem of chromatic dispersion mismatch in interferometry, especially with ultrafast sources. First, we demonstrate the origin of these artifacts through the self-phase modulation of ultrafast pulses due to focusing elements in the beam path. Next, we present three solution paradigms for DISCOTECA: optical, optoelectronic, and computational, along with quantitative comparisons to traditional methods to highlight the improvements to the dynamic range and axial profile. We explain the piecewise reconstruction of the phase mismatch between the arms of the spectral-domain interferometer using a modified short-term Fourier transform algorithm inspired by spectroscopic OCT. Finally, we present a decision-making guide for evaluating the utility of DISCOTECA in interferometry and for the artifact-free reconstruction of OCT images using an ultrafast supercontinuum source for biomedical applications.

INTRODUCTION

Low-coherence interferometry is among the most ubiquitous techniques for metrology due to its simplicity and versatility in design. From material characterization to biomedical applications, interferometric detection of broadband light can generate axially sectioned high-resolution three-dimensional images of the backscattered light. In biomedicine, the widely used implementations of low coherence interferometry are optical coherence tomography (OCT) and microscopy (OCM). OCT/OCM has evolved beyond structural imaging to include functional imaging capabilities[1] such as elastography,[2,3] angiography,[4] spectroscopy,[5] and polarimetry.[6]

While initially touted as the optical analog to pulse-echo ultrasound,[7] the spatial resolution of OCT/OCM has rapidly improved in the last two decades to achieve sub-micron spatial resolution, both laterally and axially.[8] Additionally, OCT/OCM is highly conducive to multimodal imaging systems[9] due to its relatively simple design. Multimodal systems have combined OCT/OCM with techniques such as multiphoton microscopy[10,11] (MPM), fluorescence lifetime imaging microscopy (FLIM),[12–14] and photoacoustic microscopy.[15] The advances in both ultra-high-resolution[16] (UHR) OCT/OCM and multimodal imaging[17–19] were enabled by innovations in optical sources for microscopy. Since the axial resolution of OCT/OCM is inversely proportional to the coherence length and, therefore, the spectral bandwidth of the light source,[20] there has been a strong focus on utilizing the principles from nonlinear optics for spectrally ultra-broad sources.

The advent of photonic crystal fibers (PCFs)[21–23] and supercontinuum (SC) sources, which are capable of broader spectral bandwidths, has aroused wide interest in the OCT community due to their increased axial resolution in low-coherence imaging.[24–28] Engineering PCFs for their dispersion profile, core diameter,[29] and birefringence[30,31] can further make the output SC customizable to meet different needs depending on applications. For example, all-normal dispersion (ANDi) PCFs were shown to provide octave-spanning and relatively flat SC spectra while being pulse-preserving and highly coherent. Moreover, commercial SC sources spanning hundreds of nanometers in bandwidth have been developed with turn-key operation and low-maintenance features, enabling applications in clinical OCT imaging. The use of ultrafast SC sources is also common in multimodal systems combining MPM, FLIM, or Raman scattering microscopy with OCT/OCM.[13,14,32]
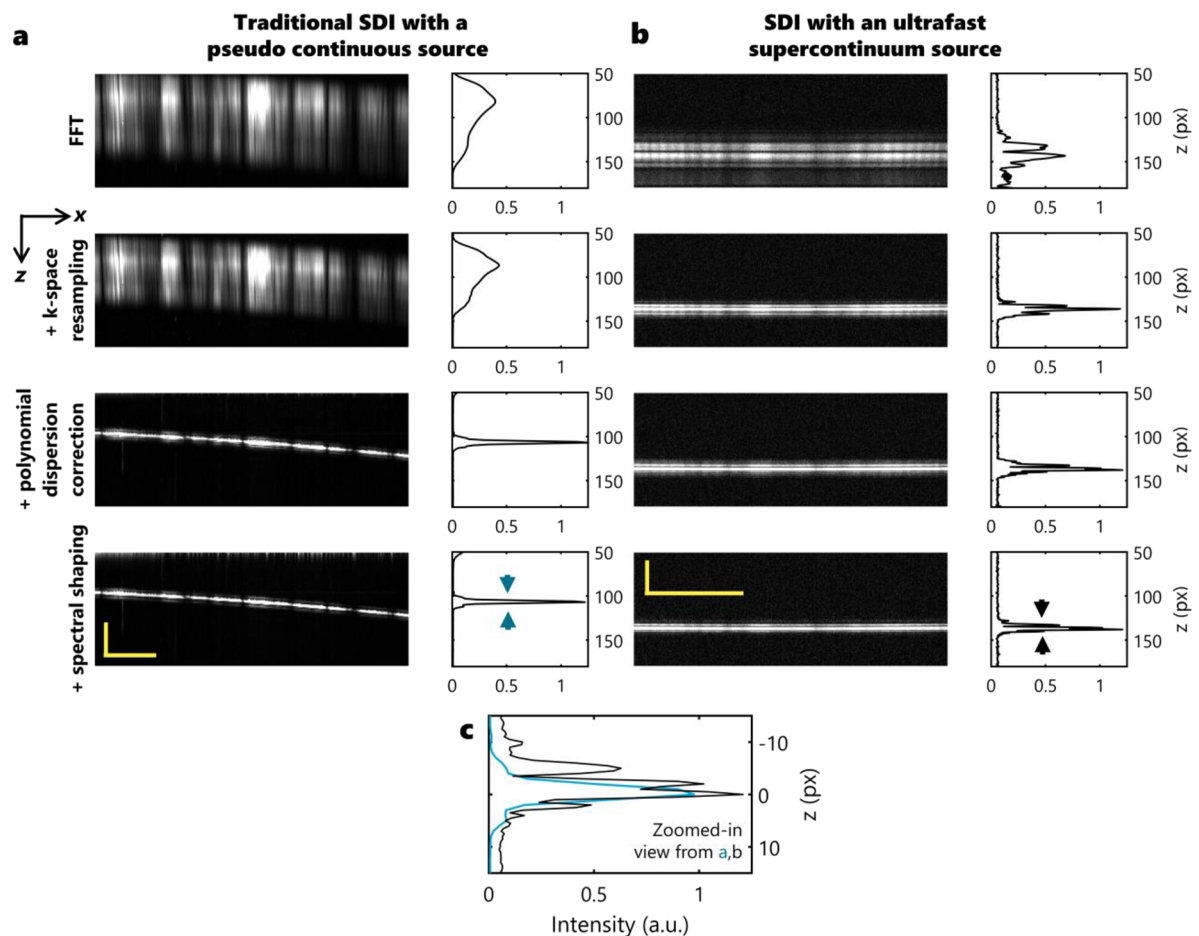

FIG. 1. Limitations of existing techniques to correct artifacts along the axial profile of OCT images from spectral-domain interferometry (SDI) with ultrafast sources. (a) and (b) The OCT/OCM images reconstructed in the spatial domain from the spectral domain with a fast Fourier transform (FFT) after no preprocessing of the raw spectrograms (first row), k-space resampling (second row), both k-space resampling and polynomial dispersion correction (third row), and k-space resampling, polynomial dispersion correction, and spectral shaping. The images in (a) were acquired on a system using a SLD source, and the images in (b) were acquired on a system with an ultrafast SC source. The average axial profiles of the OCM intensity are provided on the right. (c) Axial profiles of the last rows zoomed-in from the SLD-based (blue) and the SC-based (black) OCT setups, showing abnormal axial profiles in the SC-based images from the presence of multiple peaks. Scale bars: 100 μm.

The major disadvantages of using SC as an OCT source, however, arise from the irregular (not smooth and asymmetric) spectral shape of the spectrum and the intensity noise. Most of the commercial SC sources use a nonlinear optical fiber pumped with long pulses (e.g., in a picosecond regime), whose spectral broadening is initiated by the nonlinear amplification of quantum noise[23,33] and, therefore, the SC is intrinsically noisy. Pumping a PCF, especially an ANDi PCF, in the femtosecond (fs) regimes could provide low-noise SC[34] since the initial broadening through self-phase modulation (SPM) is known to be coherent;[23] however, complexities such as polarization instability,[35,36] Raman scattering effects, and pump laser noise can still impede the low-noise and coherent performance. On the other hand, the femtosecond-pumped PCF-based SC generally has an irregular spectral shape inherently from the interplay of third-order dispersion (TOD) and nonlinear effects including SPM, four-wave mixing, and Raman scattering effects. This is unfavorable for OCT/OCM systems, affecting the axial point-spread function (PSF). Evidence of such abnormal PSF has been found in multiple previous SC-based UHR OCT works from other groups.[37–41] Most broadband sources, including SCs and the popularly used super luminescent diodes (SLDs) with multiple independent gain media, have irregular spectral shapes. The effect of irregular pulse shapes on the reconstructed images is often corrected computationally in post-processing. Generally, the spectrum is normalized to a Gaussian or Gaussian-like profile using curve-fitting and/or deconvolution to suppress any fringes in the Fourier space during image reconstruction and improve the axial point-spread function.[42–45]

Besides spectral shaping, computational correction algorithms used to reconstruct OCT/OCM images with axially invariant transform-limited PSF (AI-TL-PSF) are spectral resampling and dispersion mismatch compensation. The former is required because the pixel-to-spectrum map for most spectrometers is defined as a function of the wavelength (λ), whereas OCT/OCM requires the pixel numbers of the spectrometer to be linearly spaced wavenumbers ($k = 2\pi/\lambda$) to ensure a Fourier transform pair between the spectral and spatial domains.[46,47] The latter is used in OCT/OCM systems where the second and third-order dispersion in the sample and reference arms are unequal and not physically matched. Typically, a polynomial or piecewise phase function of the wavenumber is multiplied by each A-scan before Fourier transformations as a digital compensation for the dispersion mismatch.[48–51] This estimation of these polynomial weights can either be performed manually or
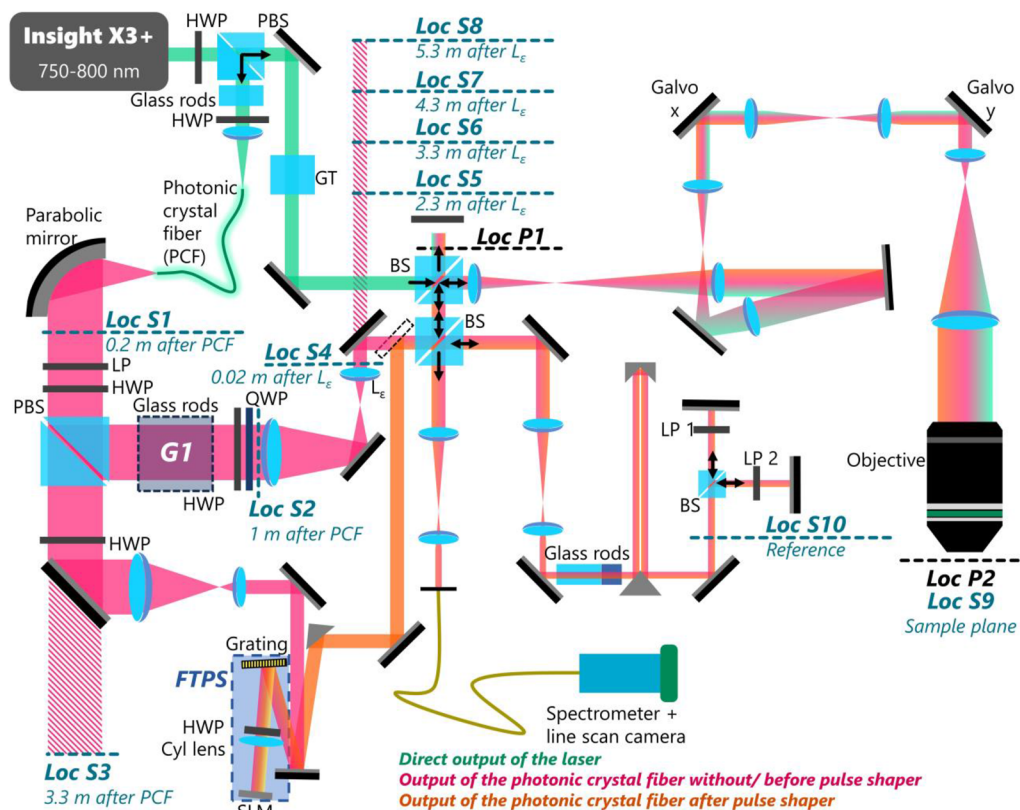

FIG. 2. Schematic of the experimental setup used in this paper for testing the origin of the atypical dispersion and testing the three solutions in the paper (see Methods). Locations P1 and P2 indicate the points where the pulse widths were measured with an autocorrelator, shown in Figs. 3 and S1. Locations S1–S10 indicate the points along the beam path where the spectral profiles were measured using an optical spectrum analyzer (OSA) (shown in Figs. 3 and S2). Location G1 indicates where a glass rod was inserted on the source side to stretch the optical pulse in time. (HWP: Half wave plate, QWP: Quarter wave plate, Cyl lens: Cylindrical lens, SLM: Spatial light modulator, PBS: Polarizing beam splitter, GT: Glan–Thompson polarizer, LP: Linear polarizer, BS: Beam-splitter cube).

automated. Most "generic" computational dispersion compensation algorithms seek to automatically derive a polynomial function by maximizing a sharpness factor[52] or by matching the axial profiles of a glass surface placed at two different optical path distances that are at the two conjugate planes.[53] In each of these cases, the demonstrations were with sources with pulse widths greater than a few dozen picoseconds, where the weights were diminishing with the higher orders. In a traditional spectral-domain OCT/OCM (SD-OCT/OCM) system using a pseudo-continuous broadband source, these steps yield a transform-limited axial profile [Fig. 1(a)] when imaging a flat surface like a glass-air interface. Each additional step in reconstruction, k-space resampling, dispersion correction, and spectral shaping helps improve the axial profile of the reconstructed images. These steps are typical in OCT reconstruction and, together, are expected to yield AI-TL-PSFs. In the context of this paper, a pseudo-continuous source refers to a light source with low temporal coherence, a large frequency bandwidth, and a duty cycle greater than 50%, such as an SLD.

Since OCT/OCM systems using SC and fs sources are relatively recent, compared to the algorithms designed for pseudo-continuous sources, traditional computational algorithms are inadequate to obtain an AI-TL-PSF. As seen in Figs. 1(b) and 1(c), unlike a pseudo-continuous-source-based system, the SC-based OCT/OCM system has artifacts along the axial direction that are not handled by traditional methods of OCT/OCM reconstruction and that are not corrected at the end of the typical processing steps that worked on the typical OCT system in Fig. 1(a). An early application of ultrafast sources for OCT was in quantum OCT, which inherently generated even-order dispersion-canceled images.[54] Quantum OCT also contains artifacts between each pair of real surfaces and requires long exposure times. Chirped pulse interferometry, using ultrafast pulsed sources, emerged as the classical analog to quantum OCT, which offered cancellation of even-ordered dispersion.[55] Nonetheless, these setups were typically operated with perfectly balanced sample and reference arms. When dispersion was introduced and later canceled, there were similar fringe artifacts observed along the axial direction.[56,57] Considering the emerging relevance of low-coherence interferometry and OCT/OCM using such ultrafast SC sources, there is a need to understand the origin of these artifacts, recognize the fallibilities of existing methods of image reconstruction, and propose new generalizable solutions to solve this issue.

This paper details a previously unreported origin of dispersion mismatch from a chromatic anomaly in OCT/OCM systems using ultrafast SC sources (Fig. 2). First, we experimentally establish the atypical dispersion of ultrafast pulses traveling through our microscope by measuring the spectral shape and pulse width at different locations in the setup at different wavelengths. We also note that the nonlinear optical interactions leading to this anomaly also affect the spectral shape. Second, since existing algorithms are

insufficient to correct this dispersion mismatch, we propose three diverse solutions: optical, optoelectronic, and computational, collectively called DISCOTECA (DISpersion COrrection Techniques for Evident Chromatic Anomaly). Finally, we describe a general algorithm for OCT/OCM systems to ascertain whether and which of these correction algorithms are needed to obtain images with AI-TL-PSFs. Together with DISCOTECA, these concepts can facilitate the process of designing, developing, and implementing novel ultra-high-resolution and multimodal OCT/OCM systems.

RESULTS

On the origin of the observed chromatically atypical dispersion mismatch

Certain assumptions are made in each step of OCT image reconstruction. We investigated which of these assumptions were inadequate to correct these artifacts to find the physical causes of the anomaly. First, a fundamental assumption in OCT/OCM is that the wavenumber (k) is analogous to the axial component of the wavevector (k_z) and is the Fourier transform pair of the axial location of the scatterer (z). For a low-NA OCT system, this assumption is valid for a large axial range. For higher NA systems, the scatterers away from the focal plane may have contributions from the radial wavevectors to the measured wavenumbers; however, near the focal plane, k_z can still be assumed to be analogous to k.[58] Second, since most spectrometers have non-uniform sampling along k, the spectrograms must be interpolated to have linear spacing in k to make them amenable for Fourier transformations. Typically, the calibration from pixel to wavelength is provided as a third- or fourth-order polynomial function, $\beta(\lambda)$. Since the systems used in Figs. 1(a) and 1(b) shared the same spectrometer and resampling algorithms with identical calibration factors, one could omit k-space resampling as the cause of this anomaly. Third, it is typically assumed that second and third-order dispersion coefficients in the Taylor series expansion, called group delay dispersion (GDD) and TOD, respectively, are the major cause of the mismatch between the sample and reference arms of an interferometer due to the different optical elements used in the sample and reference arms. Consequently, a phase profile that is a polynomial function of the wavenumber is imparted to the spectrogram to approximate this dispersion mismatch. Fourth, for the traditional methods of spectral shaping, it is assumed that the spectral profile of the interference between the sample and reference arms is equivalent to the self-interference of the reference beam (typically called the background spectrum in OCT/OCM). A popular method for spectral shaping is reshaping the background spectrum to an equivalent Gaussian with a normalization factor derived from the background spectrum. These steps can be mathematically summarized as the typical OCT/OCM reconstruction operation defined in the following equation:

$$E_{OCM}(x,y,z) = \mathcal{F}_{k \to z}\left\{ \begin{array}{l} \mathcal{N}(k) \times \exp\left(-j\left(\alpha_2(k-k_0)^2 + \alpha_3(k-k_0)^3 + \alpha_4(k-k_0)^4 + \alpha_5(k-k_0)^5\right)\right) \\ \times \mathcal{R}_{\beta(\lambda) \to k}\{-\text{Background} + I_{\text{Detected}}(x,y,\beta(\lambda))\} \end{array} \right\}, \tag{1}$$

where I_{Detected} is the spectrogram captured at the transverse coordinates x and y along the polynomial function of λ, $\beta(\lambda)$, provided as the pixel-to-wavelength map by the manufacturer. The background is acquired by blocking the incident beam on the sample arm and capturing the spectrogram of the self-interference of the spectrometer or by taking the median spectrum of I_{Detected} along x and y. The term $\mathcal{R}_{\beta(\lambda) \to k}$ is the resampling operator to convert the background subtracted spectrogram from being linearly spaced along $\beta(\lambda)$ to linearly spaced along k. The dispersion compensation is defined by the polynomial phase function, $\sum_{n=2}^{5} \alpha_n (k - k_0)^n$, by tuning the α_{2-5} coefficients (k_0 is the center wavenumber). The term $\mathcal{N}(k)$ is the spectral shaping factor, and $\mathcal{F}_{k \to z}$ denotes the Fourier transform from the k to z domain. For OCT/OCM with an ultrafast SC source, we concluded that these artifacts must be a consequence of these assumptions made in dispersion mismatch correction and spectral shaping.

To check the anomaly in the dispersion profile, we measured the pulse widths at two locations (Loc P1 and P2 in Fig. 2, following the "teal" beam path) with varying wavelengths of the laser output and under two GDD pre-compensation conditions [Figs. 3(a) and 3(b)]. Loc P1 is approximately where the SC source splits into the sample arm and the reference arm, and Loc P2 is at the

sample plane. Regardless of the GDD pre-compensation, we observed an overall increase in pulse width with an increase in wavelength at the sample plane (Loc P2) and an opposite trend at Loc P1 with some fluctuations. Note that the measured beam was directly from the laser output and had sufficient average power, so the fluctuations in measurements were not due to the lack of input power to the auto-correlator. With a larger GDD pre-compensation, the pulse width at the sample plane was shorter and had an overall smoother curve for the change of wavelength. The corresponding location at Loc P1 was longer and appeared irregular. In the other case, where the GDD pre-compensation from the laser was smaller, the trend of pulse width with wavelength appears more irregular. We estimated the GDD between Loc P1 and P2 using the relation[59] $\tau_s = \tau_{TL} \sqrt{1 + \left((4 \ln 2) GDD/\tau_{TL}^2 \right)^2}$, where τ_s and τ_{TL} refer to the stretched and transform-limited pulse width of a beam with a Gaussian spectrotemporal shape. The estimated overall GDD between P1 and P2 was plotted against the wavelength in Fig. 3(b), which could not be fit to a low-order polynomial function of wavelength (Fig. S1). This suggests that the spectroscopic refractive index cannot be approximated to the second- and third-order terms of the Taylor series expansion. One possible cause could be self-phase modulation from nonlinear interactions along the beam path due to repeated
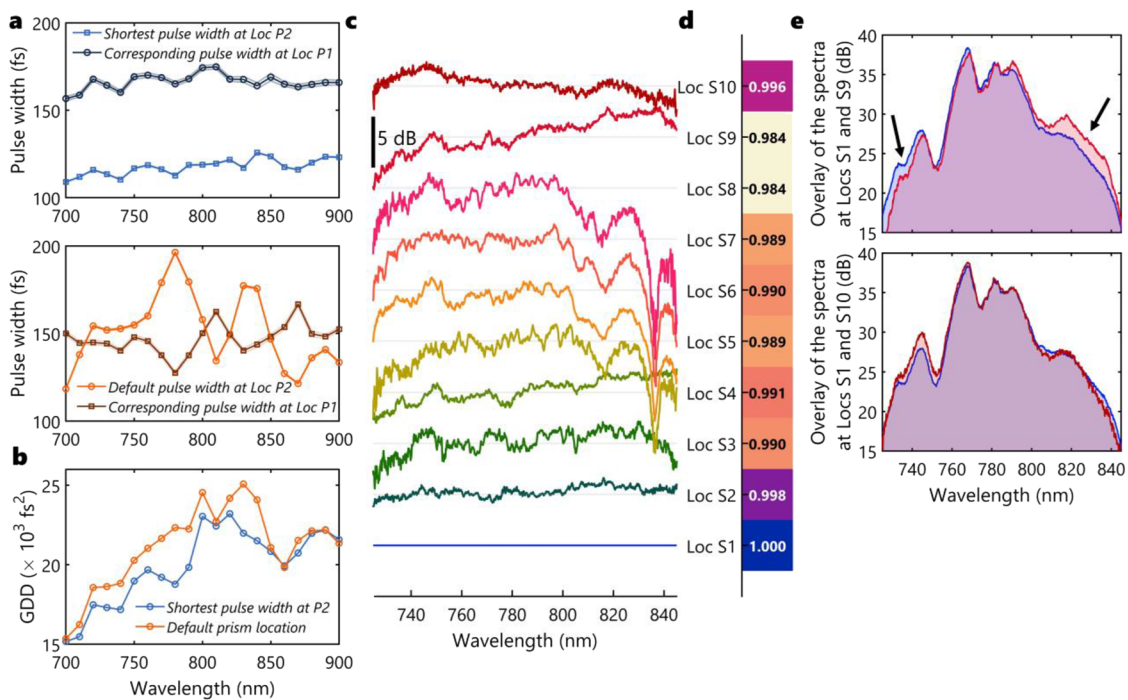

FIG. 3. Observed differences in the spectral shape and phase during propagation within the optical setup. (a) Pulse widths of the tunable beam output of the laser (teal beam path) measured at P1 (light) and P2 (dark) for the default location of the prism in the dispersion tuning module of the laser (orange) and the ideal prism location for the shortest pulse width at P2 (blue). (b) Estimated GDD values between locations P1 and P2 from the shortest pulse width measurements at P2 (blue) and for the default prism location (orange). (c) The spectra measured at locations S1–S10 normalized to S1 and expressed in dB, where S9 and S10 are at the sample and reference planes, respectively. (d) Correlation coefficient of the spectral profiles at each location with respect to location S1, highlighting the progressively decreasing correlation between S2 and S9 as the beam travels through several optical elements within the setup. (e) Overlay of the sample (S9, in red) and reference (S10, in deep red) spectral with respect to the source spectra (S1, in blue), where the arrows highlight the regions where the differences in the spectral shapes are apparent. The signal levels were measured relative to the average noise between 1000 and 1400 nm on the optical spectrum analyzer.

focusing and collimation in the sample arm that is not replicated in the reference arm.[60]

Besides temporal profile variations during propagation, we also observed changes to the spectrum. We measured the SC beam spectrum at 10 locations (indicated as Loc S1–S10 in Fig. 2, following the "pink" beam path), with Loc S1 being the output of the PCF and Loc S9 and Loc S10 being the sample plane and the end mirror of the reference arm, respectively. There were no lenses between Loc S1 and S3. Loc S4 was immediately after the first 4-f telescope in the SC beam path after the PCF. Loc S5–S8 were at various distances from the location before the beam entered the Michelson interferometer for OCM (before splitting into sample and reference arms). In Fig. S2, each spectrum was normalized to its maximum value. In Fig. 3(c), the spectra were then normalized to those at the output of the PCF (Loc S1). We observed different extents of variations in the spectral amplitude profile at all locations. Minimal differences were observed at Loc S2 or S3 between Loc S1. This might be due to propagation only through air and only for a short distance. At Loc S4, which had a pair of mirrors, a pair of lenses, and two polarization retardation plates in the beam path from Loc S1, the changes were still mild yet more obvious compared to Loc S2 and S3. More drastic spectral variations were found at Loc S5–S8. More amplitude fluctuations were observed in the shorter wavelength range (730–790 nm), and relative amplification of the signals at longer wavelengths (815–840 nm) was also observed at the same time. More importantly, the spectrum at the sample plane (Loc S9) differs from the spectrum measured at the end mirror of the reference arm (Loc S10). These differences were quantified by cross-correlation of the source spectrum with every spectrum between S1 and S10 [Fig. 3(d)]. The correlation coefficients gradually decrease from S1 to S9 as the beam propagates through the optical setup, with minimal changes between S5 and S8, where the beam propagates in free space only. The reference spectra are more closely correlated with the source spectra due to the fewer optical elements encountered during propagation. The correlation coefficient between every pair of spectra is given in Fig. S2. The differences between the normalized spectra are highlighted in the overlays shown in Fig. 3(e).

These results highlight that the atypical dispersion resulting from the differences in self-phase modulation from the nonlinear light–matter interactions along the beam propagation causes a spectroscopic change to both the amplitude and phase of the optical field that cannot be approximated as low-order polynomials. Therefore, the assumption necessary for computational dispersion correction using Eq. (1) is no longer valid. In this scenario, the initial assumption for spectral shaping is also not valid since the changes to the spectral profiles are different for the sample and reference arms of the Michelson interferometer. DISCOTECA presents three avenues for this problem: an optical and an optoelectronic solution to minimize these effects physically, and a computational solution to measure and negate these effects during image reconstruction.

Computational solution

Since the spectral shape and phase of the interferogram cannot be inferred from the background spectrum or interpolated as a polynomial, respectively, these must be derived from the interferogram itself. Borrowing from the principles of spectroscopic OCT, we describe a solution for piecewise reconstruction of both the amplitude and phase mismatch from this atypical dispersion. A series of OCM images of a flat glass surface is reconstructed by setting α_2 and α_3 to be zero in Eq. (1) and $\mathcal{N}(k)$ to be a narrow Gaussian window centered at different wavelengths [Figs. 4(a) and 4(b)]. For each image, the peak location and intensity are estimated. Ideally, for obtaining AI-TL-PSFs, the peak locations must have a constant value for every spectral window [Figs. 4(c) and 4(d)]. Therefore, using the time-shifting property of the Fourier transform, a linear phase factor is estimated for each spectral window to obtain an overall phase correction factor, $\alpha_{DISCOTECA}(k)$, through piecewise superposition at the appropriate spectral window using the same Gaussian window [Fig. 4(e)]. Rather than using the background as the reference for spectral shaping, the intensity at the peak obtained in the previous step is used to obtain the new spectral shaping coefficient, $\mathcal{N}_{DISCOTECA}(k)$. With $\alpha_{DISCOTECA}(k)$ and $\mathcal{N}_{DISCOTECA}(k)$, one can define a more general form of OCT/OCM reconstruction,

$$
\begin{aligned}
E_{OCM}(x,y,z) = \mathcal{F}_{k \to z} \Big\{ & \mathcal{N}_{DISCOTECA}(k) \times e^{-j(\alpha_{DISCOTECA}(k))} \\
& \times \mathcal{R}_{\beta(\lambda) \to k} \{ -\text{Background} + I_{\text{Detected}}(x,y,\beta(\lambda)) \} \Big\}.
\end{aligned}
$$
(2)

Equation (2) does not rely on the validity of our previous assumptions on dispersion compensation or spectral shaping in Eq. (1) and can, therefore, account for the atypical dispersion profile of the ultrafast SC laser and the differences in the changes to the spectral profiles in the sample and reference beams. Additionally, since the nonlinear effect responsible for this chromatic anomaly is expected to be sensitive to the polarization of this incident beam,[21–23] the artifacts were observed to be different for the two polarization states (Fig. S3). Therefore, the factors were estimated separately for two orthogonal polarization states of the beam in the setup. The drift of the peak location, the peak intensity, and the dispersion compensation phase were all starkly different for the two polarization states [Figs. 4(c)–4(e)]. The recovery of artifact-free images for the ultrafast SC-based system is also shown in Fig. S3.

The generalizability of the solution in Eq. (2) can be observed when using it for a pseudo-continuous-source-based OCT/OCM setup [Figs. 4(f)–4(h)]. As expected in the case of normal dispersion, the peak location drift was nearly linear within the entire spectral region, and there were no abrupt undulations to the spectral profiles. Unlike the ultrafast SC-based system, the spectral profiles of the background of the pseudo-continuous-source-based OCT/OCM setup matched closely to the peak intensity values (Fig. S4). The image metrics used in this paper are the signal-to-noise ratio (SNR), the dynamic range (DR), and the width of the axial profile (see "Methods" for details). For most samples, the DR, which is based on percentiles of the intensity values, describes the improvement to the background suppression from the computational algorithm better and is less sensitive to the bias from unnaturally bright pixels within the sample.

The images in Fig. 4(i) demonstrate that the $\alpha_{DISCOTECA}(k)$ and $\mathcal{N}_{DISCOTECA}(k)$ estimated for this setup yield reconstruction with AI-TL-PSFs, which lead to an increase in the SNR by ~6 dB. This generalizability is discussed in detail in the later sections. This computational solution was compared against an exhaustive polynomial search, which was optimized for the axial width and peak of the
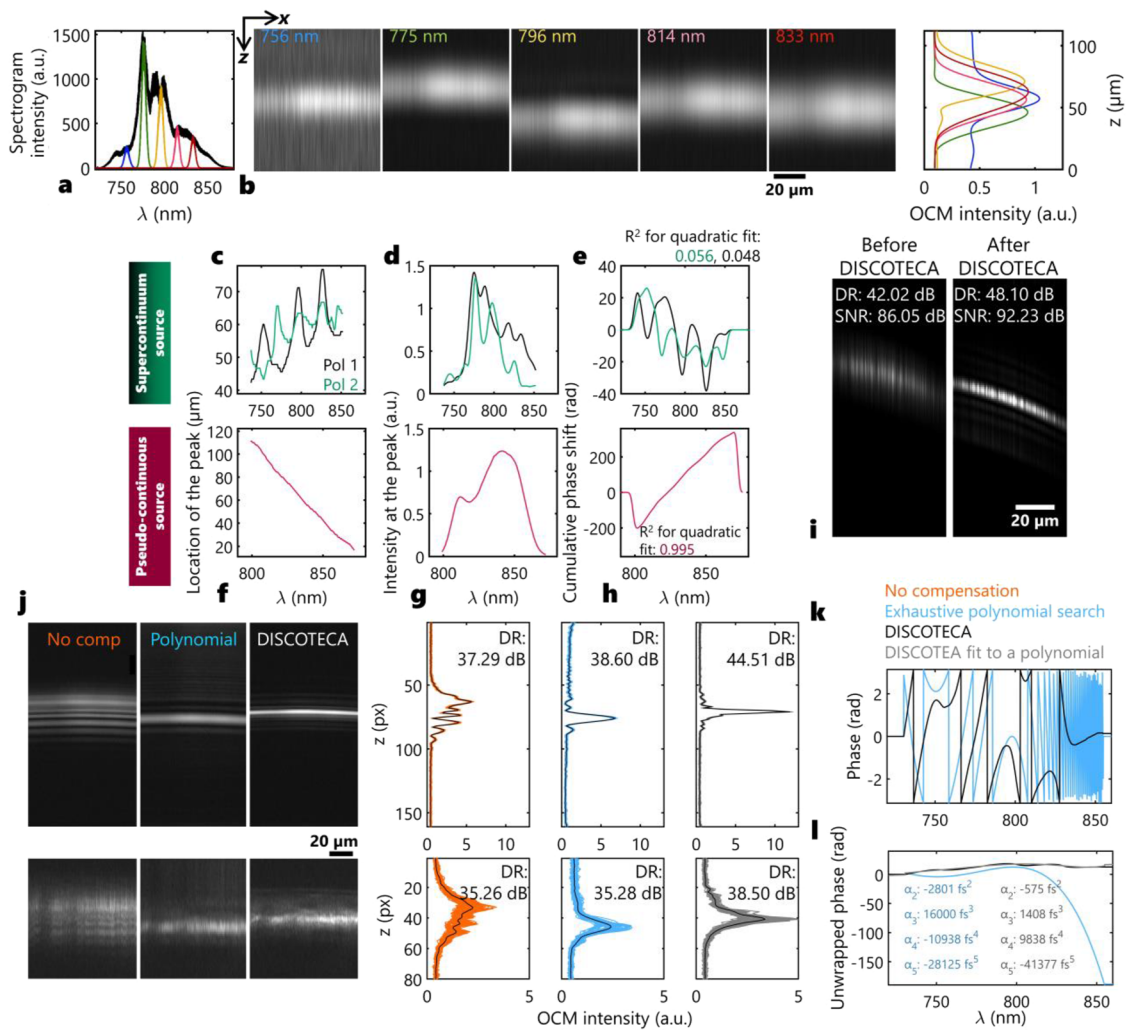
FIG. 4. Principles and demonstration of the computational solution of DISCOTECA. (a) Shorter spectral windows centered at 756 nm (blue), 775 nm (green), 796 nm (yellow), 814 nm (orange), and 833 nm (red) within the full spectrogram captured (black) from a glass surface in an ultrafast SC-based OCT/OCM setup. (b) OCM cross-section (*x*–*z*) images reconstructed from the shorter spectral windows shown in (a), with the mean axial profile plotted in the right column. (c) and (f) Axial location of the peak for each shorter spectral window chosen during reconstruction at the two polarization states of an ultrafast SC-based OCT/OCM setup (c) and a pseudo-continuous-source-based OCT/OCM setup (f). (d) and (g) The peak intensity of the glass surface in the OCT/OCM images reconstructed for each shorter spectral window chosen during reconstruction at the two polarization states of an ultrafast SC-based OCT/OCM setup (d) and a pseudo-continuous-source-based OCT/OCM setup (g). (e) and (h) Estimated cumulative phase offset evaluated piecewise as the slope of the phase ramp required in the spectral domain to displace the axial location of the peak to a constant value for every chosen spectral window within the entire spectrum at the two polarization states of an ultrafast SC-based OCT/OCM setup (e) and a traditional OCT setup (h). (i) Cross-section of the images after applying the computational solution of DISCOTECA based on Eq. (2) for the pseudo-continuous-source-based OCT/OCM setup. The SNR and DR for the two reconstructions are listed within each panel. (j) Cross-section images of glass surfaces (top) and a section of mouse tail (bottom), averaged over 20 B-scans from adjacent locations (corresponding to 10 μm) for the three cases: no correction, polynomial correction from exhaustive search, and DISCOTECA (in order) for the SC-based OCM setup. The DR is listed in dB within each plot. (k) Compensation phase profiles used in Eqs. (1) and (2) based on the exhaustive polynomial search (blue) and DISCOTECA (black). (l) Unwrapped equivalent phase from (j), along with the fifth-order polynomial fitting for the DISCOTECA-derived phase profiles. The coefficients are listed in the plots.

Gaussian fit to the axial profile of a glass surface [Fig. 4(j)]. While the polynomial search yielded significant improvements to the axial profile, the reconstructed images using DISCOTECA have both a higher peak intensity and a smaller axial width. This improvement is also apparent in the reconstruction of a mouse tail. Whereas the polynomial compensation did indeed cause an increase in the DR by 1 dB

in glass and negligible in the mouse tail, the improvement in the DR is considerably higher using DISCOTECA (7 dB in glass and 3 dB in the mouse tail). Comparing the estimated phase profiles using both methods, the similarities between the two between 760 and 810 nm are apparent [Fig. 4(k)]. However, due to the unusual dispersion in this setup, the phase compensation for beyond this range could

not be smooth enough to be modeled as a fifth-order polynomial across this range. In fact, the fit of the DISCOTECA phase profile to a fifth-order polynomial is poor [Figs. 4(l) and S5]. The polarization dependence of this artifact is apparent in Fig. S6. The 3D profiles of the glass surface show more deterioration in one polarization state than the other, although both states could be restored to the transform-limited axial resolution after correction. Movie S1 shows the computation procedures of DISCOTECA for a glass surface.

The computational solution of DISCOTECA for the two polarization states is demonstrated in Fig. 5 on freshly extracted pig skin. As seen in the cross-section images [Fig. 5(a)], the images after DISCOTECA have suppressed artifacts, particularly in polarization 2. The 3D reconstruction of the tissue under each processing condition indicates clear distortions to the structures that appear to blur structures at each depth. This is restored after correction. This improvement was quantified as improvements to the axial width (Gaussian fit) and DR. Similar to the results for the glass surface (Fig. S6), the DR improvement in polarization 1 (3.06 dB) is higher than that of polarization 2 (1.55 dB). The improvement to the

estimated axial width was also higher for polarization 1 (2.35×) than polarization 2 (1.36×). This biases the ratiometric analysis of the polarization-sensitive scattering. Whereas the skin at this collagen-rich layer is expected to be birefringent, the polarization ratio at the plane 10 px below the surface appears biased toward lower values due to the artifacts before correction with DISCOTECA [Fig. 5(b)]. These differences are highlighted in Fig. 5(c) through the histogram of the intensity ratio in each depth. In a sample such as pig skin, where the collagen fibers are aligned, one would expect a linear gradual change to the birefringence, where the peak ratio of intensities will change monotonically along depth. This improvement is only apparent after correction with DISCOTECA. Movie S1 shows the computation procedures of DISCOTECA for a glass surface. Similar improvements to quantitative imaging with OCT/OCM are observed in other tissue samples (Figs. S7 and S8). Even though the PCF output displayed polarization-dependent spectral amplitude profiles (Fig. S9), the output first passed a linear polarizer at a fixed angle that maximized the power output before the QWP converted the beam into a circular polarization. The differences in the artifacts between the two polarizations mainly came from propagation.
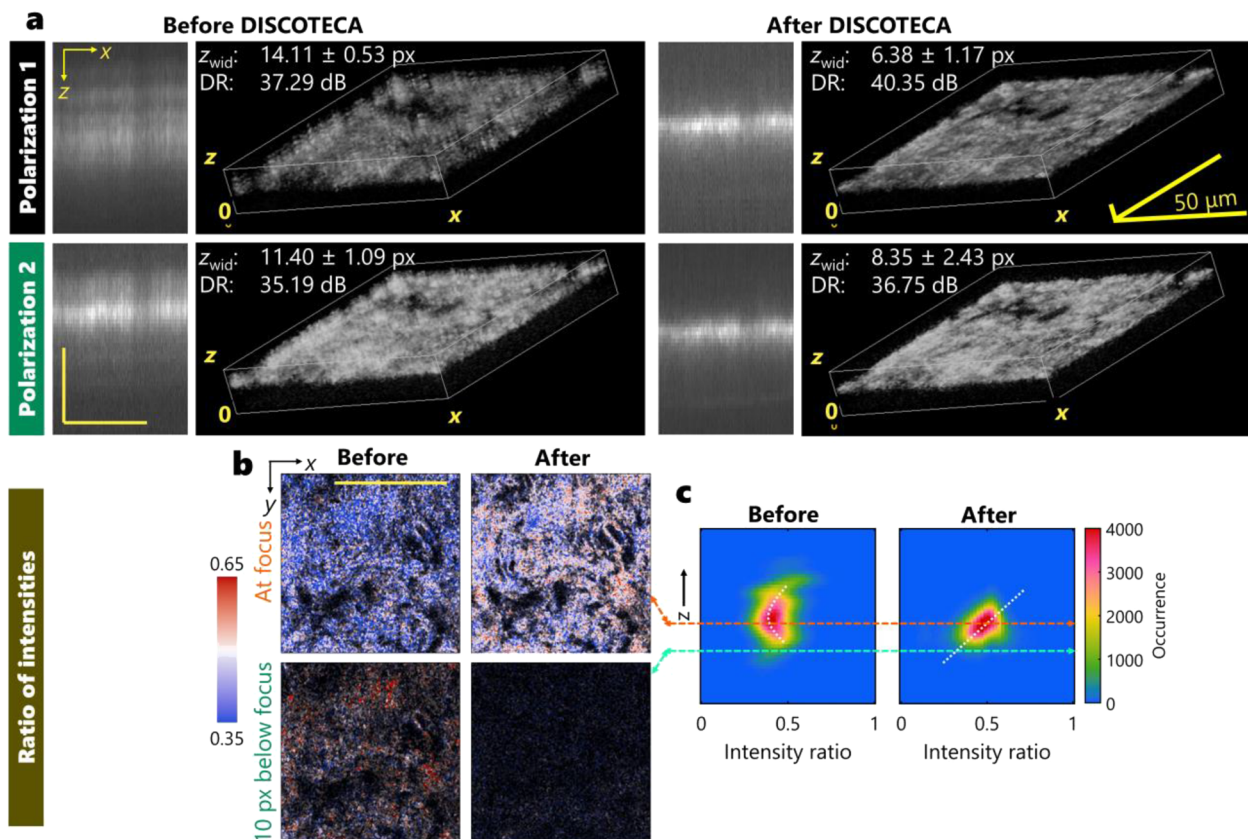

FIG. 5. Demonstration of computational solution for DISCOTECA on tissue samples. (a) Cross-section (bottom) and 3D reconstruction of pig skin captured 30 μm (focal plane) below the surface at the two polarization states before and after DISCOTECA. The DR and the average width (Gaussian fit) are indicated within each panel. (b) and (c) Ratio of the intensities at two planes at and below focus before and after correction with DISCOTECA (b) and the corresponding histograms at each depth, where the two lines indicate the depth from which the panels in (b) were derived. All scale bars: 50 μm.

Optical and optoelectronic solutions

Since most of the artifacts arise from the ultrafast nature of the incident light, we theorized that changing the phase of the light source entering the interferometer can change the corresponding dispersion profiles. In its simplest implementation, the temporal pulse width can be extended by passing the beam through a glass rod (assuming normal dispersion within this spectral range). We tested that in the setup in Fig. 2 by inserting a glass rod (SF11, 4-in. long) at location G1. Note that this location is at the source arm of the interferometer and not at the reference arm, where one typically employs glass rods or elements to address the dispersion mismatch. The beam size at this location was larger (12 mm in diameter) than the rest of the setup; the lower irradiance is expected to minimize the nonlinear

effects within the glass rod itself. The pulse width with and without the glass rods was 1 ps and >3 ps, respectively. Figure 6(a) shows a section of mouse tail imaged with the setup with and without a glass rod at G1, with no dispersion and spectral shape correction, with polynomial correction (up to third order) of the dispersion and Gaussian normalization of the spectra from the background, and with the correction from DISCOTECA. At increased pulse widths, the polynomial and DISCOTECA corrections are expected to be more similar. This is apparent in the axial profiles at a1 and a2 highlighted for the cross-section images shown in Fig. 6(a). Note that the dispersion correction helps recover weakly scattering features away from the focal plane with both polynomial and DISCOTECA corrections (in a1). Both solutions help localize features to a narrower set
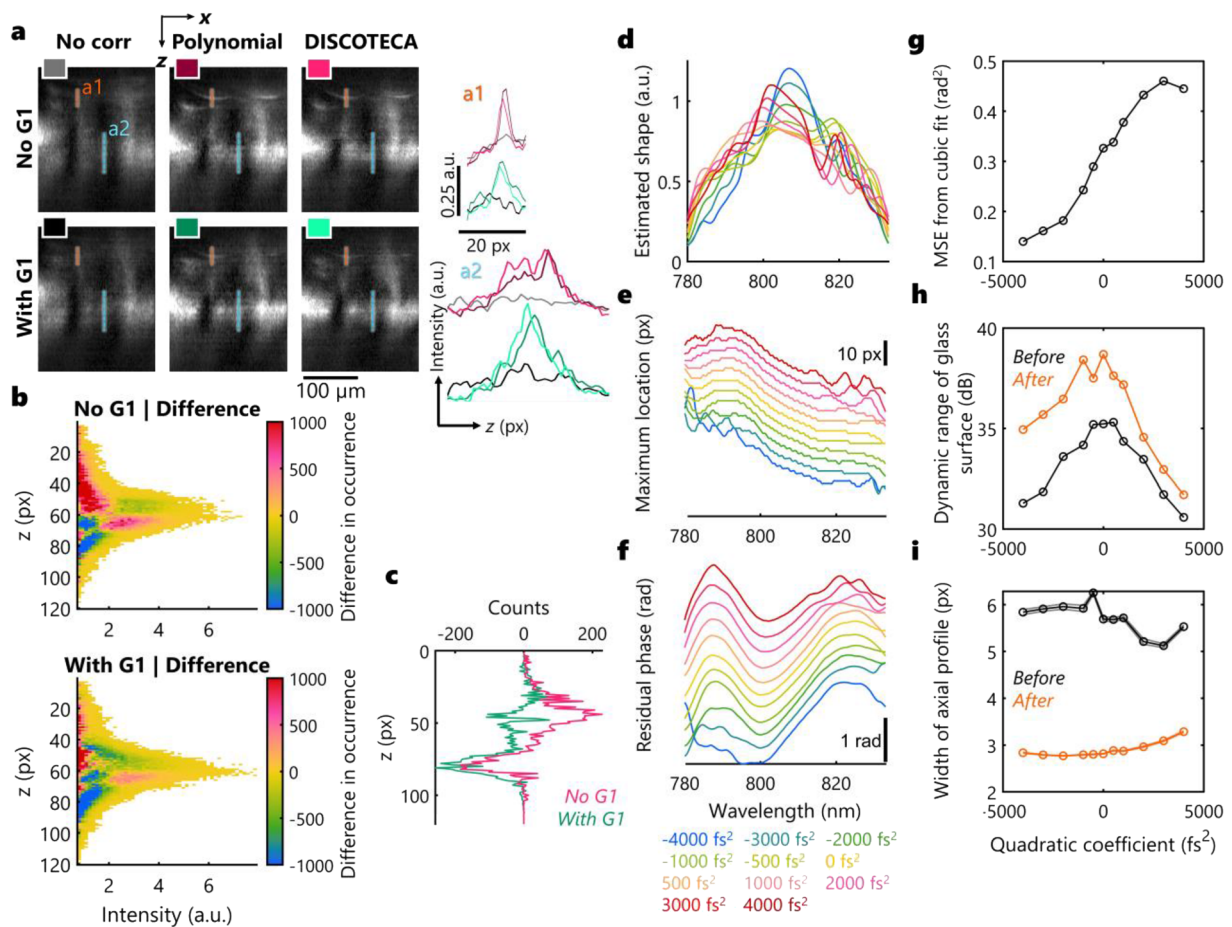

FIG. 6. Optical and optoelectronic solutions of DISCOTECA. (a) Cross-sectional OCT/OCM images of mouse tail with and without inserting a glass rod at location G1 in Fig. 2. In each optical configuration, three reconstructions are presented, corresponding to no correction, polynomial correction up to the third order, and correction with the piecewise spectral normalization and phase from DISCOTECA. The axial profile along the two lines (orange: a1 and blue: a2) is plotted to the left. The color box within each cross-sectional plot corresponds to the color of the adjacent plots. (b) The difference between the histograms of the OCM intensity at each plane for the polynomial correction and DISCOTECA without (above) and with (below) the glass rod at G1. (c) The mean difference in the occurrence counts for the histogram heatmap in (b) at each depth, without (pink) and with (cyan) the glass rod at G1. (d) Estimated spectral shape of the interferogram from DISCOTECA. (e) Estimated maximum location of the peak axially for each pattern on the pulse shaper estimated from DISCOTECA. (f) Corresponding residual phase (after subtracting the second- and third-order dispersion) obtained from (e). (g) The mean square error between the cubic fit to DISCOTECA plotted against the quadratic coefficient of the SLM pattern to modulate the pulse width imparted on the FTPS. (h) DR and (i) the width of the axial profiles plotted against the quadratic coefficient.

of planes (Fig. S10). However, in a2, the polynomial correction without glass rods is quite different from that of DISCOTECA, where a higher signal is recovered across a larger depth range. This improvement was quantified using the differences in the histograms of the intensities at each depth between the polynomial and DISCOTECA solutions for each optical configuration, shown in Fig. 6(b) [see Figs. S11(a) and S11(b)]. Visually, there is a larger difference in the counts both above and below the focal plane without the glass rods, despite minimal differences to the DR [Fig. S11(c)]. The mean difference in counts is also larger at most depths above the focus without the glass rods [Fig. 6(c)]. On average, the setup with the glass rod had fewer count differences across all depths (42 counts) than the setup without the glass rod (50 counts). These differences in intensities do not arise from a monotonic shift to the axial plane during reconstruction [Fig. S11(d)].

These results highlight that the polynomial correction better approximates the correction from DISCOTECA when the pulse width at the source is larger (causing a reduced abnormal dispersion mismatch). An extreme case of this is presented in Fig. S12, where the output of the PCF was coupled into a 1-m-long single-mode fiber before sending it into the interferometer, in the setup described previously by Iyer *et al.*[13] The dispersion mismatch appears to be mostly quadratic. Additionally, unlike the poor-fit to a polynomial in Fig. 4(k), the fit here is good ($R^2 = 0.984$), suggesting the suppression of the unusual dispersion and validating that the anomalous effects described in the previous sections are indeed from the propagation of the sub-ps pulses through the setup.

We assumed that the change in the spectral phase and amplitude observed in Fig. 3 was a consequence of using an ultrashort pulse with an atypical phase at Loc P1. The optical solution of using a glass rod only adds second-order dispersion that results in stretching the pulse, which could reduce the magnitude of the nonlinear effects observed along beam propagation. However, an optoelectronic solution enables arbitrary changes to the optical phase. In this solution, we used a custom-built Fourier transform pulse shaper (FTPS), which has been described previously.[61] We used a polarizing beam splitter to split the output of the PCF, and one path was directed into the FTPS, whose output was then used as the phase-shaped SC source for OCM. We encoded a phase function, $\phi(\omega) = a_2(\omega - \omega_0)^2$, with a_2 being the second-order dispersion term. The pulse from the PCF could be compressed to 220 fs if the quadratic coefficient on the SLM was 12 000 fs^2 (Fig. S13). However, the intensity was also reduced and insufficient for OCM at higher compression. For the results in Fig. 6, we varied the a_2 parameter from −4000 fs^2 to 4000 fs^2 and collected OCM data for a glass surface. The overall envelope of the background [Fig. S14(a)] and the total energy across the entire spectral bandwidth [i.e., the area under the curve of the intensity profile, Fig. S14(b)] were consistent, indicating phase modulation of the FTPS induced minimal loss to the beam intensity in any spectral region.

The spectral shape of the interferogram from the piecewise estimation showed slight differences in the location of the peak and at higher wavelengths [Fig. 6(d)]. We also tracked the location of the peak in the axial profile across different wavelengths [Fig. 6(e)] and observed more undulations to the location of the peak at the higher wavelengths at smaller pulse widths (higher a_2). However, the

estimated phase varied from the polynomial fit (third order) for each pulse width [Figs. 6(f) and S14(c)]. However, the mean square error (MSE) between the polynomial and piecewise phases shows that the deviation is higher at shorter pulse widths. After correction, the DRs could all be improved by 3–4 dB approximately [Fig. 6(h)], and the axial widths could be reduced from 6 to 3 pixels [Fig. 6(i)] estimated from the axial profiles shown in Fig. S14(d). These results highlight the ability of the optoelectronic solution to effectively suppress the artifacts from abnormal dispersion within the interferometer.

A decision chart for reconstruction in low coherence spectral-domain interferometry

As shown in Fig. 4, the piecewise reconstruction of the dispersion phase mismatch and spectral shaping coefficients are applicable both for pseudo-continuous-source-based OCT/OCM and ultrafast SC-based OCT/OCM setups. However, as demonstrated in Fig. 6, a combination of multiple solutions of DISCOTECA could yield better results. It is also important to note that the reduction in the correlations between the spectral shapes is very low in Fig. 3(d). Therefore, it may be difficult to estimate the need for DISCOTECA simply from differences in the spectral shapes at the source, reference, and sample planes. With the increasing diversity of sources for OCT/OCM, we describe a method to quantitatively evaluate the need for the solutions offered by DISCOTECA in Fig. 7. We chose to fit the central region of $\alpha_{DISCOTECA}(k)$ (the spectral regions where $\mathcal{N}_{DISCOTECA}(k)$ is above the noise floor) to a quadratic polynomial and calculated the goodness of fit (R^2 value). For the results in Fig. 4, the R^2 value was 0.995 for the pseudo-continuous-source-based OCT/OCM setup and ~0.05 for the ultrafast SC-based OCT/OCM setup. This suggests that a simple polynomial approximation for dispersion compensation for the former is sufficient, whereas, for the latter, the computational solution of DISCOTECA is needed to recover AI-TL-PSFs. Compared to polynomial correction, the estimation of the phase and spectral shape correction in this paper improved the DR and axial widths consistently, even if the changes to the structures were subtle. DISCOTECA was also less dependent on the hyperparameters. In the piecewise estimation algorithm, there were two hyperparameters—the width and number of windows. Figures S15–S17 show the peak locations, phase profiles, normalization function, and the axial profiles with the DR and estimated widths for different combinations of the hyperparameters. For a large range of windows and widths, the DR and estimated axial widths were remarkably consistent, with no noticeable asymmetries in the axial profiles, highlighting the adaptability of the algorithm. The piecewise estimation only needs one traversal through all spectral windows, though there is a Fourier transform required at each step. However, these steps are computationally efficient on most programming platforms. For a window size of 100, the average time for estimation was computed to be 10.2 + 0.5 s in MATLAB (Mathworks Inc.) performed on a Windows PC (Intel i9, 2 GHz, 64 GB RAM). Additionally, Fig. S18 shows different combinations of the processing steps, similar to Fig. 1, showing the critical role played by spectral shaping and dispersion correction for optimal image reconstruction.
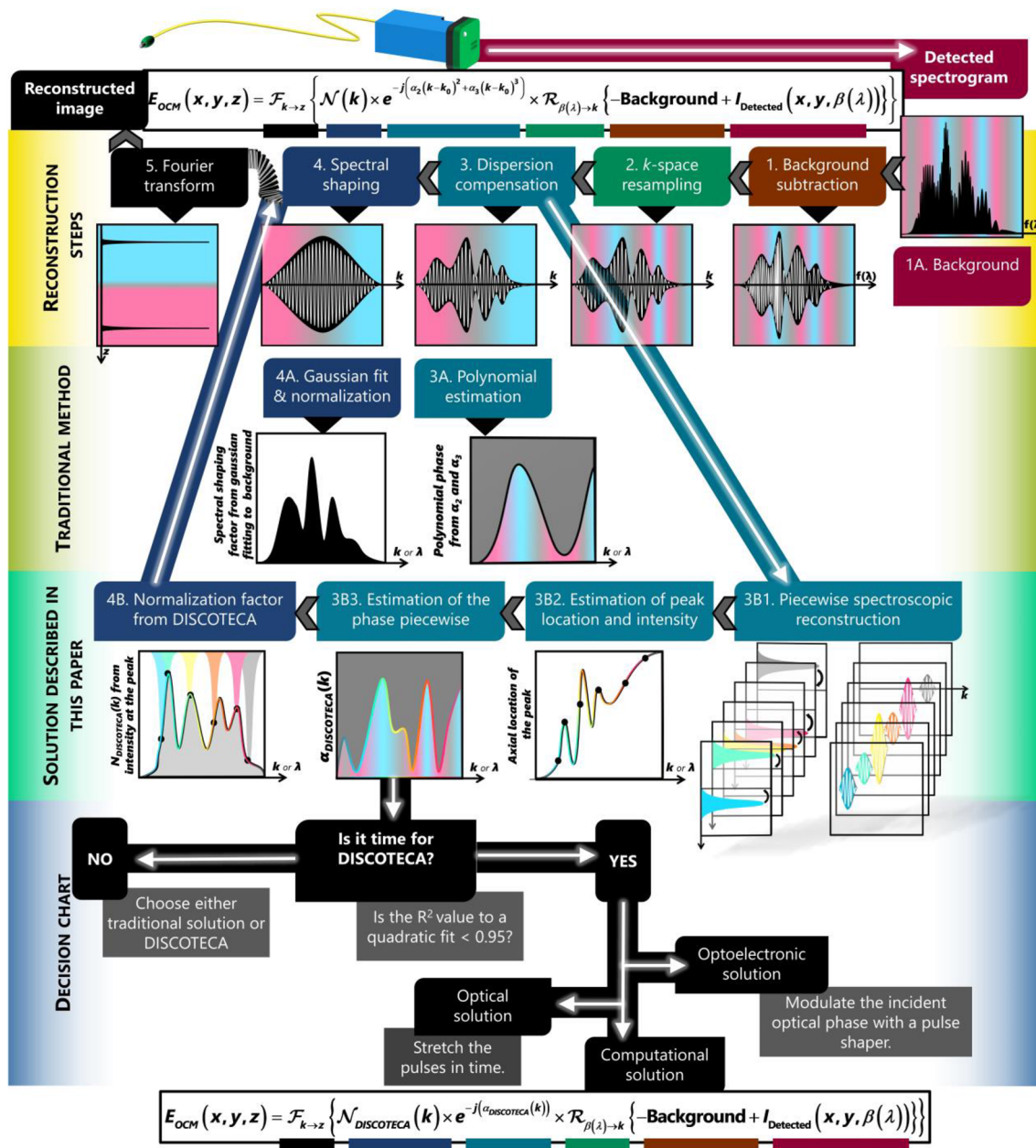
FIG. 7. A decision chart for reconstruction in low coherence spectral-domain interferometry. The first two describe the typical steps in OCT reconstruction, the second row describes the traditional algorithm for estimation of the spectral shape normalization factor and dispersion correction phase, and the third row describes the estimation of these parameters using the piecewise estimation method described in this paper, and the bottom row describes the decision guide for evaluating the need for DISCOTECA. The pink-to-blue heatmaps indicate the phase of the complex-valued profiles. The equations in the figures are reiterated in Eqs. (1) and (2) in the paper.

DISCUSSION

Artifacts were observed in reconstructed OCT/OCM images sourced by an ultrafast SC laser that were due to unusual dispersion, which was not apparent in SLD-based OCT systems. We presented three solution paradigms in this paper, out of which the computational solution or a combination of the computational solution with either the optical or optoelectronic solution yielded the best results. Therefore, an argument could be made to further extend our optical solution to generate pseudo-continuous pulses by stretching it

further to nanosecond pulse widths (by passing it through hundreds of meters of fibers), which would introduce unwanted attenuations to the source. Adding meters of glass rods is not a practical solution either. Spatial light modulator (SLM)-based pulse shapers have a limit on the amount of GDD that can be added based on the pixel spectral width and the performance of the SLM during phase wrapping. An alternative solution is to change the Michelson interferometer configuration to a Linnik interferometer;[62] however, the sample arm with specialized optical elements such as deformable mirrors and objective lenses cannot be cost-efficiently reproduced in the reference arm identically. Having a glass element at G1 (in Fig. 2) to stretch the pulse from the femtosecond to the picosecond regime along with the computational solution provides a balance between the methods. An extension to this could be to modulate the spectral phase of the light entering the PCF to minimize the atypical dispersion. However, this could affect the spectral broadening characteristics of the fiber and affect image quality, such as the axial resolution.

While many SC-based UHR-OCT studies have reported a similar issue with axial PSF, as shown in Fig. 1(b), very few have discussed the reason or provided a solution. Gonzalo *et al.* attributed the artifacts in the axial PSF to SPM during the SC generation process.[37,63] Using the SC generated through an ANDi fiber, the OCT system was found to have higher sensitivity than using a commercial SC laser but a worse axial PSF profile. In our case, the PCF was pumped at a wavelength within the 750–800 nm range, and the generated SC never crossed the zero-dispersion wavelength of the fiber, which can be considered to be operating in an all-normal dispersion condition, similar to the case of an ANDi fiber. To solve the artifacts originating from the SPM-related spectral amplitude oscillations, external spectral shaping elements can be introduced either before[64] or after[65] the SC generation. The polarization dependence of this artifact, as shown in Fig. 4, can be attributed to the interplay of both the polarization mode dispersion in the fiber and the polarization-sensitive nonlinear processes that govern the SC generation, such as SPM. Note that the SC source was circularly polarized before splitting into the sample and the reference arm. The differences in the spectral phase profile or the wavelength-dependent dispersion profile of each individual polarization originated from the SC source itself.

A consequence of the artifact is its effect on quantitative imaging with OCT/OCM. In this paper, we show a simple example of ratiometric imaging for polarimetry. A more important need for precise axial localization is phase-based processing for OCT/OCM, specifically computational adaptive optics and interferometric synthetic aperture microscopy. Both techniques rely on having complex-valued AI-TL-PSF images as precursors to their algorithms. These artifacts create a superposition of scatterers from multiple axial planes onto a single *en face* image plane, thereby distorting the optical phase. This distortion will render computational adaptive optics using digital wavefront correction ineffective. Interferometric synthetic aperture microscopy requires resampling the complex-valued intensities in 3D k-space; the incorrect phase mismatch in the *k*-space will yield incorrect resampling and digital refocusing. The DISCOTECA solutions presented in the paper will be used for wavefront sensing and adaptive optics applications in the future. Such a windowing approach to correct the spectral shape was utilized by Chen *et al.* to reduce sidelobes.[66] Rather than

obtaining a single spectral normalization factor for a calibration surface and using it for all applications, this method required multiple B-scan reconstructions at different spectral windows and further rank order filtering for each reconstruction. Additionally, Fig. S18 shows how the artifacts are dominated not by the spectral shape but by the phase dispersion derived from DISCOTECA.

FTPS techniques are known to provide precise controls over the spectral phase profile and are capable of spectral amplitude modulations. The FTPS used in this study was custom-made with a total cost of $15 000 (predominantly for the spatial light modulator). The FTPS was more tunable compared to the glass-rod in the source, which reduced the artifacts in the OCT images by using a pulse with a larger width. Despite the additional cost, the FTPS is uniquely tunable, where one can instantaneously switch between different pulse profiles, which is advantageous in multimodal imaging.[61,67,68] With the increasing utility of FTPS techniques for commercial metrology and biomedical imaging applications,[69,70] DISCOTECA also describes a new technique for estimating the spectral phase and dispersion parameters with fewer assumptions and hardware resources than techniques such as spectral phase interferometry for direct electric-field reconstruction[71] (SPIDER) or multiphoton intra-pulse interference phase scan[72] (MIIPS). Both SPIDER and MIIPS measured the signals generated from second-order parametric processes in certain nonlinear crystals. With low-coherence sources that are favorable for OCT, the efficiency of these nonlinear interactions is lower and, therefore, can affect the accuracy because of the deficient signal-to-noise ratio. While DISCOTECA does not require prior calibration steps, SPIDER relies on the precise calibration of the time delay, which may again require spectral interferometry measurement that involves a reference to a known phase. However, it also has its limitations. In the demonstration shown in Fig. 6, even though FTPS phase modulation resulted in a more linear relationship between axial PSF location and center wavelength, without the computational DISCOTECA method, it alone could not correct for the dispersion mismatch. For future studies, a MIIPS-like iterative algorithm could be implemented to estimate the spectral phase profile of the source more accurately. Multimodal quantitative imaging is a rapidly expanding field in biophotonics, and single-source optical systems have a high potential for clinical translation. On a similar note, the utility of ultrafast lasers for interferometric detection has been accelerating in nonlinear and quantum optics[73] research applications and for metrology in surface profiling[74–76] and distance measurements.[77]

In conclusion, we investigated the dispersion mismatch in OCT/OCM systems based on ultrafast SC sources, unveiled a chromatic dispersion anomaly that significantly impacts the axial PSF and, therefore, the image quality, and proposed a novel and all-encompassing solution, namely DISCOTECA. Nonlinear optical interactions such as SPM were hypothesized as contributing factors to this anomaly. Although it was technically challenging to validate the hypothesis of SPM being the major underlying cause of the dispersion mismatch, this work focused on developing practical solutions incorporating optical, optoelectronic, and computational strategies that can effectively mitigate the chromatic dispersion mismatch in low-coherence light interferometry and achieve artifact-free image reconstruction. This work provides a systematic approach to evaluate the dispersion profile in low-coherence interferometry systems and effectively correct for non-polynomial

dispersion mismatches. This approach is especially beneficial for ultra-high resolution OCT systems using SC laser sources and highly complex multimodal OCT systems using ultrafast lasers. With the ability to achieve artifact-free high-contrast interferometric imaging, we believe that DISCOTECA can further advance the field of biomedical imaging as well as quantum optics and metrology.

METHODS

System setup and data acquisition

We use a tunable titanium-sapphire laser (Insight X3+, Spectra Physics) as the excitation source for our imaging system. We previously described a similar setup for multimodal imaging with two-photon fluorescence lifetime imaging microscopy, second harmonic generation microscopy, and polarization-sensitive OCM.[13,14,68] The laser was tuned to different central wavelengths of 750–800 nm and operated at 80 MHz. As seen in Fig. 2, there were three possible beam paths for excitation at the sample plane. The "teal" path is the direct output of the laser, which is typically used for multiphoton excitation in this setup during multimodal operation. In the context of this paper, it was utilized for pulse width measurements at various parts of the entire OCM spectrum. A part of the beam is used to pump a PCF (LMA-PM-5, NKT Photonics) for an output power of 300 mW and a bandwidth of 150–200 nm (base-to-base), which yields an axial resolution of about 2 μm. Typical OCT/OCM systems have an axial resolution of 5–10 μm, whereas the current setup is comparable to a UHR OCT/OCM setup. The spectral broadening depends on the excitation wavelength, the dispersion of the pulses before the fiber, and the polarization. The polarization and dispersion before the fiber were optimized for each excitation wavelength for maximum coupling efficiency and the best spectral shape (least spiky features or amplitude oscillations according to spectrometer measurements). The output of the PCF is collimated with a parabolic mirror for an initial beam diameter of 12 mm and linearly polarized with a linear polarizer. This beam is either directed into the interferometer directly after passing through a quarter wave plate with 0.2× magnification or directed to a custom pulse shaper using a polarizing beam splitter and a half-wave plate. The measurements of the spectral profiles were made using the former. The procedure for designing and calibrating the pulse shaper is described in Yang et al.[61] Polarization-sensitive OCM was enabled using polarization delay multiplexing in the reference arm previously described in Iyer et al.[13] The beam is scanned by a pair of galvanometer mirrors (6220H, Cambridge Technology) and focused through a 1.05 NA, 25× objective lens (XLPLN25XWMP2, Olympus Inc). The interferogram was captured using a fiber-based spectrometer (Cobra S 800, Wasatch Photonics) and one of two line scan cameras (OctoPlus, Teledyne e2v; or Sprint spL4096-140 km, Basler Inc.). The line-scan cameras were operated typically at 40 or 80 kHz A-scan rates at the maximum exposure times for the respective scan rates. NBK-7 glass plates totaling 1.25 in. were placed in the reference arm to minimize the dispersion mismatch between the sample and the reference up to a point, beyond which DISCOTECA was needed. The typical SNR of a glass surface after all reconstruction was measured to be 92 dB, with less than 1 dB variance between A-scans within a $10 \times 10~\mu m^2$ region.

The traditional OCT system consisted of a superluminescent diode centered at 850 nm (Super-Lum), a fiber beam splitter, a fiber-based spectrometer (Cobra S 800, Wasatch Photonics), and a line scan camera (Sprint spL4096-140 km, Basler Inc.). The beam is scanned by a single axis galvanometer mirror (Thorlabs) and focused through a 50-mm focal length achromatic doublet lens. A glass block (BK7) was placed in the reference arm to create a dispersion mismatch for comparison.

A custom LabVIEW (NI) acquisition software was used to acquire the data, with custom C-based programs to control the digitizer and the GPU module. A queue buffer is set up on LabVIEW to asynchronously pass each line from the digitizer memory to the GPU memory via the RAM. A GPU (Titan X, NVIDIA Corporation) was used for real-time display. The raw spectrograms are buffered into a file and stored for postprocessing later.

All pulse width measurements were made using a microscopy autocorrelator (Carpe, APE, Berlin DE). The estimated pulse width was demodulated and fit to a Gaussian function to estimate the pulse width using the fit() function in MATLAB. All spectral measurements in Fig. 3 were made with an optical spectrum analyzer (OSA202C, Thorlabs Inc.) with the DR within the bands shown to be above 20 dB.

Data analysis

The images were processed in MATLAB (Mathworks Inc.). The parameters for polynomial dispersion compensation were tuned manually for the best axial resolution of the glass surface. The spectral normalization factors, $\mathcal{N}(k)$ and $\mathcal{N}_{DISCOTECA}(k)$, were performed by fitting the normalized background spectrum or the normalized peak intensity values to a Gaussian using the fit() function of MATLAB and deriving the ratio of the equivalent Gaussian spectrum to the normalized background or the normalized peak intensity, respectively, with a regularization factor of 0.2 in the denominator. $\alpha_{DISCOTECA}(k)$ was derived from the piecewise phase function described in the previous section and multiplied with a constant factor for scaling, which was calibrated manually to give the best peak-to-trough ratio and axial resolution. For the results in Figs. 3 and 4, the number of windows was kept approximately equal to the bandwidth of the source (in nm), and the width of the window was chosen to be 2-nm wide (corresponding to 19 wide in Figs. S15–S17). Both the spectral windows and the evaluation of $\alpha_{DISCOTECA}(k)$ and $\mathcal{N}_{DISCOTECA}(k)$ were performed on the k-space resampled spectrogram to avoid any artifacts from nonuniform sampling.

The exhaustive polynomial search was performed in MATLAB by an iterative multidimensional binary search, with the objective function being the minima of the Gaussian width, the maxima of the Gaussian amplitude, and the goodness of fit (R^2) being over 0.5. The range for searching for the orders was $\pm[10^4, 10^5, 10^6, 10^7~fs^5]$ for α_{2-5}. The searching was iterated with smaller step sizes until each of the weights was below 10. The overall estimation cycled through 48 020 combinations, which took 42 min.

The DR was estimated as the ratio of the 98th and second quartiles of the intensities in the image. The width of the axial profiles was estimated by fitting the profiles to a Gaussian function. The volumes were rendered using the Volume Viewer plugin in (FIJI, ImageJ).

Sample preparation

The tissues were extracted from rats and mice postmortem after asphyxiation using CO_2, followed by cervical dislocation. The tissues were surgically resected and placed in an imaging dish with a clear glass bottom coverslip (P35G-1.0-14-C, MatTek) containing ~100 μl of freshly prepared 1× phosphate-buffered saline and placed on ice until imaging. The pig skin was obtained from a local butcher, and the fresh hide was acquired at the beginning of the day, right after slaughter. A small square was cut from the back skin after preliminary hair removal using clippers and a razor.

SUPPLEMENTARY MATERIAL

See the supplementary material for Movie S1 and the supplemental figures S1–S18.

AUTHOR DECLARATIONS

Conflict of Interest

The pulse shaper described in this study has been disclosed to the Office of Technology Management as an intellectual property of L.Y., R.R.I., J.E.S., and S.A.B. The authors declare no other conflicts of interest.

Ethics Approval

All animal procedures were conducted in accordance with protocols approved by the Illinois Institutional Animal Care and Use Committee at the University of Illinois at Urbana-Champaign and in compliance with the ARRIVE guidelines.

Author Contributions

R.R.I. and L.Y. contributed equally to this work.

Conceptualization: R.R.I., L.Y., S.A.B.; Data curation, methodology: R.R.I., L.Y., J.E.S.; Formal analysis, software, validation, writing original draft, and visualization: R.R.I., L.Y.; Writing reviewing and editing: R.R.I., L.Y., J.E.S., E.J.C., D.R.S., S.A.B.; Resources: E.J.C., D.R.S.; Supervision and funding acquisition: S.A.B.

Rishyashring R. Iyer: Conceptualization (lead); Data curation (equal); Formal analysis (equal); Investigation (equal); Methodology (equal); Software (equal); Validation (equal); Visualization (equal); Writing – original draft (equal); Writing – review & editing (equal). **Lingxiao Yang**: Conceptualization (lead); Data curation (equal); Formal analysis (equal); Investigation (equal); Methodology (equal); Software (equal); Validation (equal); Visualization (equal); Writing – original draft (equal); Writing – review & editing (equal). **Janet E. Sorrells**: Data curation (equal); Methodology (equal); Software (equal); Writing – review & editing (equal). **Eric J. Chaney**: Resources (equal). **Darold R. Spillman, Jr.**: Project administration (equal); Resources (equal). **Stephen A. Boppart**: Conceptualization (equal); Funding acquisition (equal); Project administration (equal); Supervision (equal); Writing – review & editing (equal).

DATA AVAILABILITY

The raw data that support the findings of this study are available from the corresponding author upon request and through a collaborative research agreement. The codes used to acquire and process the images are available in the "Repository upon publication." No new materials were generated in this study.

REFERENCES

[1] J. Kim, W. Brown, J. R. Maher, H. Levinson, and A. Wax, "Functional optical coherence tomography: Principles and progress," Phys. Med. Biol. **60**(10), R211–R237 (2015).

[2] J. A. Mulligan, G. R. Untracht, S. N. Chandrasekaran, C. N. Brown, and S. G. Adie, "Emerging approaches for high-resolution imaging of tissue biomechanics with optical coherence elastography," IEEE J. Sel. Top. Quantum Electron. **22**(3), 246–265 (2016).

[3] K. V. Larin and D. D. Sampson, "Optical coherence elastography—OCT at work in tissue biomechanics [Invited]," Biomed. Opt. Express **8**(2), 1172 (2017).

[4] R. F. Spaide, J. G. Fujimoto, N. K. Waheed, S. R. Sadda, and G. Staurenghi, "Optical coherence tomography angiography," Prog. Retinal Eye Res. **64**, 1–55 (2018).

[5] H. S. Nam and H. Yoo, "Spectroscopic optical coherence tomography: A review of concepts and biomedical applications," Appl. Spectrosc. Rev. **53**(2–4), 91–111 (2018).

[6] B. Baumann, "Polarization sensitive optical coherence tomography: A review of technology and applications," Appl. Sci. **7**(5), 474 (2017).

[7] D. Huang, E. A. Swanson, C. P. Lin, J. S. Schuman, W. G. Stinson, W. Chang, M. R. Hee, T. Flotte, K. Gregory, C. A. Puliafito, and J. G. Fujimoto, "Optical coherence tomography," Science **254**(5035), 1178–1181 (1991).

[8] W. Drexler, "Ultrahigh-resolution optical coherence tomography," J. Biomed. Opt. **9**(1), 47 (2004).

[9] R. A. Leitgeb and B. Baumann, "Multimodal optical medical imaging concepts based on optical coherence tomography," Front. Phys. **6**, 114 (2018).

[10] B. W. Graf, A. J. Bower, E. J. Chaney, M. Marjanovic, S. G. Adie, M. De Lisio, M. C. Valero, M. D. Boppart, and S. A. Boppart, "*In vivo* multimodal microscopy for detecting bone-marrow-derived cell contribution to skin regeneration," J. Biophotonics **7**(1–2), 96–102 (2014).

[11] B. Jeong, B. Lee, M. S. Jang, H. Nam, S. J. Yoon, T. Wang, J. Doh, B.-G. Yang, M. H. Jang, and K. H. Kim, "Combined two-photon microscopy and optical coherence tomography using individually optimized sources," Opt. Express **19**(14), 13089 (2011).

[12] M. W. Lee, J. W. Song, W. J. Kang, H. S. Nam, T. S. Kim, S. Kim, W.-Y. Oh, J. W. Kim, and H. Yoo, "Comprehensive intravascular imaging of atherosclerotic plaque *in vivo* using optical coherence tomography and fluorescence lifetime imaging," Sci. Rep. **8**(1), 14561 (2018).

[13] R. R. Iyer, J. E. Sorrells, L. Yang, E. J. Chaney, D. R. Spillman, B. E. Tibble, C. A. Renteria, H. Tu, M. Žurauskas, M. Marjanovic, and S. A. Boppart, "Label-free metabolic and structural profiling of dynamic biological samples using multi-modal optical microscopy with sensorless adaptive optics," Sci. Rep. **12**(1), 3438 (2022).

[14] L. Yang, R. R. Iyer, J. E. Sorrells, E. J. Chaney, and S. A. Boppart, "Label-free multimodal polarization-sensitive optical microscope for multiparametric quantitative characterization of collagen," Optica **11**(2), 155 (2024).

[15] W. Zhang, Y. Li, V. P. Nguyen, Z. Huang, Z. Liu, X. Wang, and Y. M. Paulus, "High-resolution, *in vivo* multimodal photoacoustic microscopy, optical coherence tomography, and fluorescence microscopy imaging of rabbit retinal neovascularization," Light: Sci. Appl. **7**(1), 103 (2018).

[16] W. Drexler, U. Morgner, R. K. Ghanta, F. X. Kärtner, J. S. Schuman, and J. G. Fujimoto, "Ultrahigh-resolution ophthalmic optical coherence tomography," Nat. Med. **7**(4), 502–507 (2001).

[17] S. You, H. Tu, E. J. Chaney, Y. Sun, Y. Zhao, A. J. Bower, Y.-Z. Liu, M. Marjanovic, S. Sinha, Y. Pu, and S. A. Boppart, "Intravital imaging by simultaneous label-free autofluorescence-multiharmonic microscopy," Nat. Commun. **9**(1), 2125 (2018).

[18] H. Tu and S. A. Boppart, "Coherent fiber supercontinuum for biophotonics: Coherent fiber supercontinuum for biophotonics," Laser Photonics Rev. **7**(5), 628–645 (2013).

[19] H. Tu, Y. Liu, D. Turchinovich, M. Marjanovic, J. K. Lyngsø, J. Lægsgaard, E. J. Chaney, Y. Zhao, S. You, W. L. Wilson, B. Xu, M. Dantus, and S. A. Boppart, "Stain-free histopathology by programmable supercontinuum pulses," Nat. Photonics **10**(8), 534–540 (2016).

[20] *Optical Coherence Tomography: Technology and Applications*, edited by W. Drexler and J. G. Fujimoto (Springer International Publishing, Cham, 2015).

[21] T. A. Birks, J. C. Knight, and P. St. J. Russell, "Endlessly single-mode photonic crystal fiber," Opt. Lett. **22**(13), 961 (1997).

[22] J. K. Ranka, R. S. Windeler, and A. J. Stentz, "Visible continuum generation in air–silica microstructure optical fibers with anomalous dispersion at 800 nm," Opt. Lett. **25**(1), 25 (2000).

[23] J. M. Dudley, G. Genty, and S. Coen, "Supercontinuum generation in photonic crystal fiber," Rev. Mod. Phys. **78**(4), 1135–1184 (2006).

[24] A. Aguirre, N. Nishizawa, J. Fujimoto, W. Seitz, M. Lederer, and D. Kopf, "Continuum generation in a novel photonic crystal fiber for ultrahigh resolution optical coherence tomography at 800 nm and 1300 nm," Opt. Express **14**(3), 1145 (2006).

[25] H. Lim, Y. Jiang, Y. Wang, Y.-C. Huang, Z. Chen, and F. W. Wise, "Ultrahigh-resolution optical coherence tomography with a fiber laser source at 1 μm," Opt. Lett. **30**(10), 1171 (2005).

[26] N. Nishizawa, Y. Chen, P. Hsiung, E. P. Ippen, and J. G. Fujimoto, "Real-time, ultrahigh-resolution, optical coherence tomography with an all-fiber, femtosecond fiber laser continuum at 15 μm," Opt. Lett. **29**(24), 2846 (2004).

[27] B. Povazay, K. Bizheva, A. Unterhuber, B. Hermann, H. Sattmann, A. F. Fercher, W. Drexler, A. Apolonski, W. J. Wadsworth, J. C. Knight, P. St. J. Russell, M. Vetterlein, and E. Scherzer, "Submicrometer axial resolution optical coherence tomography," Opt. Lett. **27**(20), 1800 (2002).

[28] I. Hartl, X. D. Li, C. Chudoba, R. K. Ghanta, T. H. Ko, J. G. Fujimoto, J. K. Ranka, and R. S. Windeler, "Ultrahigh-resolution optical coherence tomography using continuum generation in an air–silica microstructure optical fiber," Opt. Lett. **26**(9), 608 (2001).

[29] Y. Shen, A. A. Voronin, A. M. Zheltikov, S. P. O'Connor, V. V. Yakovlev, A. V. Sokolov, and M. O. Scully, "Picosecond supercontinuum generation in large mode area photonic crystal fibers for coherent anti-Stokes Raman scattering microspectroscopy," Sci. Rep. **8**(1), 9526 (2018).

[30] J. R. Folkenberg, M. D. Nielsen, N. A. Mortensen, C. Jakobsen, and H. R. Simonsen, "Polarization maintaining large mode area photonic crystal fiber," Opt. Express **12**(5), 956 (2004).

[31] A. Ortigosa-Blanch, J. C. Knight, W. J. Wadsworth, J. Arriaga, B. J. Mangan, T. A. Birks, and P. St. J. Russell, "Highly birefringent photonic crystal fibers," Opt. Lett. **25**(18), 1325 (2000).

[32] R. R. Iyer, C. A. Renteria, L. Yang, J. E. Sorrells, J. Park, L. Sun, Z. Yu, Y. Huang, M. Marjanovic, L. M. Mirica, and S. A. Boppart, "Tracking the binding of multi-functional fluorescent tags for Alzheimer's disease using quantitative multiphoton microscopy," J. Biophotonics **15**(9), e202200105 (2022).

[33] S. Rao D, M. Jensen, L. Grüner-Nielsen, J. T. Olsen, P. Heiduschka, B. Kemper, J. Schnekenburger, M. Glud, M. Mogensen, N. M. Israelsen, and O. Bang, "Shot-noise limited, supercontinuum-based optical coherence tomography," Light: Sci. Appl. **10**(1), 133 (2021).

[34] M. Klimczak, G. Soboń, R. Kasztelanic, K. M. Abramski, and R. Buczyński, "Direct comparison of shot-to-shot noise performance of all normal dispersion and anomalous dispersion supercontinuum pumped with sub-picosecond pulse fiber-based laser," Sci. Rep. **6**(1), 19284 (2016).

[35] I. Bravo Gonzalo, R. D. Engelsholm, M. P. Sørensen, and O. Bang, "Polarization noise places severe constraints on coherence of all-normal dispersion femtosecond supercontinuum generation," Sci. Rep. **8**(1), 6579 (2018).

[36] H. Tu, Y. Liu, X. Liu, D. Turchinovich, J. Lægsgaard, and S. A. Boppart, "Nonlinear polarization dynamics in a weakly birefringent all-normal dispersion photonic crystal fiber: Toward a practical coherent fiber supercontinuum laser," Opt. Express **20**(2), 1113 (2012).

[37] M. Jensen, I. B. Gonzalo, R. D. Engelsholm, M. Maria, N. M. Israelsen, A. Podoleanu, and O. Bang, "Noise of supercontinuum sources in spectral domain optical coherence tomography," J. Opt. Soc. Am. B **36**(2), A154 (2019).

[38] S. Ishida and N. Nishizawa, "Quantitative comparison of contrast and imaging depth of ultrahigh-resolution optical coherence tomography images in 800–1700 nm wavelength region," Biomed. Opt. Express **3**(2), 282 (2012).

[39] T.-A. Wang, M.-C. Chan, H.-C. Lee, C.-Y. Lee, and M.-T. Tsai, "Ultrahigh-resolution optical coherence tomography/angiography with an economic and compact supercontinuum laser," Biomed. Opt. Express **10**(11), 5687 (2019).

[40] M. Maria, I. Bravo Gonzalo, T. Feuchter, M. Denninger, P. M. Moselund, L. Leick, O. Bang, and A. Podoleanu, "Q-switch-pumped supercontinuum for ultra-high resolution optical coherence tomography," Opt. Lett. **42**(22), 4744 (2017).

[41] S. Bourquin, A. D. Aguirre, I. Hartl, P. Hsiung, T. H. Ko, J. G. Fujimoto, T. A. Birks, W. J. Wadsworth, U. Bünting, and D. Kopf, "Ultrahigh resolution real time OCT imaging using a compact femtosecond Nd:Glass laser and nonlinear fiber," Opt. Express **11**(24), 3290 (2003).

[42] A. C. Akcay, J. P. Rolland, and J. M. Eichenholz, "Spectral shaping to improve the point spread function in optical coherence tomography," Opt. Lett. **28**(20), 1921 (2003).

[43] M. Szkulmowski, M. Wojtkowski, P. Targowski, and A. Kowalczyk, "Spectral shaping and least square iterative deconvolution in spectral OCT," in *Coherence Domain Optical Methods and Optical Coherence Tomography in Biomedicine VIII*, edited by V. V. Tuchin, J. A. Izatt, and J. G. Fujimoto (SPIE, Bellingham, 2004), p. 424.

[44] R. Tripathi, N. Nassif, J. S. Nelson, B. H. Park, and J. F. De Boer, "Spectral shaping for non-Gaussian source spectra in optical coherence tomography," Opt. Lett. **27**(6), 406 (2002).

[45] P. D. Woolliams, R. A. Ferguson, C. Hart, A. Grimwood, and P. H. Tomlins, "Spatially deconvolved optical coherence tomography," Appl. Opt. **49**(11), 2014 (2010).

[46] K. Wang, Z. Ding, T. Wu, C. Wang, J. Meng, M. Chen, and L. Xu, "Development of a non-uniform discrete Fourier transform based high speed spectral domain optical coherence tomography system," Opt. Express **17**(14), 12121 (2009).

[47] K. C. Zhou, R. Qian, A.-H. Dhalla, S. Farsiu, and J. A. Izatt, "Unified *k*-space theory of optical coherence tomography," Adv. Opt. Photonics **13**(2), 462 (2021).

[48] A. Fercher, C. Hitzenberger, M. Sticker, R. Zawadzki, B. Karamata, and T. Lasser, "Numerical dispersion compensation for partial coherence interferometry and optical coherence tomography," Opt. Express **9**(12), 610 (2001).

[49] A. L. Oldenburg and R. K. Chhetri, "Digital dispersion compensation for ultrabroad-bandwidth single-camera spectral-domain polarization-sensitive OCT," in *Optical Coherence Tomography and Coherence Domain Optical Methods in Biomedicine XV*, edited by J. G. Fujimoto, J. A. Izatt, and V. V. Tuchin (SPIE BiOS, San Francisco, 2011), p. 78891V.

[50]D. L. Marks, A. L. Oldenburg, J. J. Reynolds, and S. A. Boppart, "Digital algorithm for dispersion correction in optical coherence tomography for homogeneous and stratified media," Appl. Opt. **42**(2), 204 (2003).

[51]Q. Gong, J. Jiang, R. K. Wang, F. Zhang, and J. Yao, "Dispersion compensation methods for ultrahigh-resolution optical coherence tomography," in *Fourth International Conference on Photonics and Imaging in Biology and Medicine*, edited by K. Xu, Q. Luo, D. Xing, A. V. Priezzhev, and V. V. Tuchin (SPIE, Tianjin, China, 2006), p. 60471S.

[52]L. Pan, X. Wang, Z. Li, X. Zhang, Y. Bu, N. Nan, Y. Chen, X. Wang, and F. Dai, "Depth-dependent dispersion compensation for full-depth OCT image," Opt. Express **25**(9), 10345 (2017).

[53]K. Singh, G. Sharma, and G. J. Tearney, "Estimation and compensation of dispersion for a high-resolution optical coherence tomography system," J. Opt. **20**(2), 025301 (2018).

[54]M. B. Nasr, B. E. A. Saleh, A. V. Sergienko, and M. C. Teich, "Demonstration of dispersion-canceled quantum-optical coherence tomography," Phys. Rev. Lett. **91**(8), 083601 (2003).

[55]J. Lavoie, R. Kaltenbaek, and K. J. Resch, "Quantum-optical coherence tomography with classical light," Opt. Express **17**(5), 3818 (2009).

[56]M. Jensen, N. M. Israelsen, M. Maria, T. Feuchter, A. Podoleanu, and O. Bang, "All-depth dispersion cancellation in spectral domain optical coherence tomography using numerical intensity correlations," Sci. Rep. **8**(1), 9170 (2018).

[57]K. Ogawa and M. Kitano, "Classical realization of dispersion-canceled, artifact-free, and background-free optical coherence tomography," Opt. Express **24**(8), 8280 (2016).

[58]T. S. Ralston, D. L. Marks, P. Scott Carney, and S. A. Boppart, "Interferometric synthetic aperture microscopy," Nat. Phys. **3**(2), 129–134 (2007).

[59]J. B. Guild, C. Xu, and W. W. Webb, "Measurement of group delay dispersion of high numerical aperture objective lenses using two-photon excited fluorescence," Appl. Opt. **36**(1), 397 (1997).

[60]R. A. Fisher and W. K. Bischel, "Numerical studies of the interplay between self-phase modulation and dispersion for intense plane-wave laser pulses," J. Appl. Phys. **46**(11), 4921–4934 (1975).

[61]L. Yang, R. R. Iyer, J. E. Sorrells, C. A. Renteria, and S. A. Boppart, "Temporally optimized and spectrally shaped hyperspectral coherent anti-Stokes Raman scattering microscopy," Opt. Express **32**(7), 11474 (2024).

[62]A. Dubois, K. Grieve, G. Moneron, R. Lecaque, L. Vabre, and C. Boccara, "Ultrahigh-resolution full-field optical coherence tomography," Appl. Opt. **43**(14), 2874 (2004).

[63]I. Bravo Gonzalo, M. Maria, R. D. Engelsholm, T. Feuchter, L. Leick, P. M. Moselund, A. G. H. Podoleanu, and O. Bang, "Ultra-low noise supercontinuum source for ultra-high resolution optical coherence tomography at 1300 nm," in *Design and Quality for Biomedical Technologies XI*, edited by R. Raghavachari, R. Liang, and T. J. Pfefer (SPIE, San Francisco, 2018), p. 22.

[64]M. Song, S.-P. Han, J. Park, H. Choi, S. Kim, T. T. Tran, H. D. Kim, and M. Song, "Flat-top supercontinuum generation via Gaussian pulse shaping," Opt. Express **29**(8), 12001 (2021).

[65]W. Yuan, J. Mavadia-Shukla, J. Xi, W. Liang, X. Yu, S. Yu, and X. Li, "Optimal operational conditions for supercontinuum-based ultrahigh-resolution endoscopic OCT imaging," Opt. Lett. **41**(2), 250 (2016).

[66]Y. Chen, J. Fingler, and S. E. Fraser, "Multi-shaping technique reduces sidelobe magnitude in optical coherence tomography," Biomed. Opt. Express **8**(11), 5267–5281 (2017).

[67]J. E. Sorrells, L. Yang, R. R. Iyer, E. J. Chaney, C. A. Renteria, and S. A. Boppart, "Programmable hyperspectral coherent anti-Stokes Raman scattering microscopy," Opt. Lett. **49**(9), 2513 (2024).

[68]R. R. Iyer, J. E. Sorrells, L. Yang, E. J. Chaney, and S. A. Boppart, "VAMPIRE microscopy enables fast and simultaneous structural, metabolic, and chemical characterization of living tissues label-free," in *Multiphoton Microscopy in the Biomedical Sciences XXIV*, edited by A. Periasamy, P. T. So, and K. König (SPIE, San Francisco, 2024), p. 27.

[69]Y. Silberberg, "Quantum coherent control for nonlinear spectroscopy and microscopy," Annu. Rev. Phys. Chem. **60**(1), 277–292 (2009).

[70]D. Goswami, "Optical pulse shaping approaches to coherent control," Phys. Rep. **374**(6), 385–481 (2003).

[71]C. Iaconis and I. A. Walmsley, "Spectral phase interferometry for direct electric-field reconstruction of ultrashort optical pulses," Opt. Lett. **23**(10), 792 (1998).

[72]V. V. Lozovoy, I. Pastirk, and M. Dantus, "Multiphoton intrapulse interference. IV. Ultrashort laser pulse spectral phase characterization and compensation," Opt. Lett. **29**(7), 775 (2004).

[73]M. V. Chekhova and Z. Y. Ou, "Nonlinear interferometers in quantum optics," Adv. Opt. Photonics **8**(1), 104 (2016).

[74]J. S. Oh and S.-W. Kim, "Femtosecond laser pulses for surface-profile metrology," Opt. Lett. **30**(19), 2650 (2005).

[75]Y. Wang, S. Xiong, and G. Wu, "Femtosecond laser-based phase-shifting interferometry for optical surface measurement," Rev. Sci. Instrum. **89**(11), 113105 (2018).

[76]Y. Wang, G. Xu, S. Xiong, and G. Wu, "Large-field step-structure surface measurement using a femtosecond laser," Opt. Express **28**(15), 22946 (2020).

[77]Y. Xu, D. Liu, W. Zhou, and L. Ding, "Absolute distance measurement by spectrally resolved interferometry based on a femtosecond pulse laser," Opt. Eng. **51**(8), 081509 (2012).